Physics 4999E- Honours Thesis Project

The Cause of Variability in FeLoBAL Quasar SDSS J122933.32+262131.2

Sofia Pasquini
Supervisor: Dr. Sarah Gallagher

Draft version April 26, 2021
Typeset using LATEX default style in AASTeX63

ABSTRACT

Quasars are extremely bright, distant celestial objects powered by supermassive black holes (SMBHs) located at the centres of their host galaxies. Powerful mass outflows (gas winds moving at thousands to tens of thousands of kilometers per second) in quasars are believed to influence the interstellar medium (gaseous medium between stars) as well as rates of star-formation in their host galaxies. Although quasars have been studied for decades, the structure and kinematics in their inner regions remain poorly understood. The optical and UV spectra of quasars can provide insights into the physical conditions and structures of the outflows in the inner regions of these objects which can lead to a better understanding of the link between quasars and their host galaxies. Variability studies of quasar outflows allows for better constraints on physical conditions of the gas such as its ionization state, column density, and the position of the outflow relative to the central supermassive black hole. Iron (Fe) Low-Ionization Broad Absorption Line (FeLoBAL) quasars make up the smallest fraction of the Broad Absorption Line (BAL) quasar subtype, which encompasses all quasars which have broad absorption features which are significantly blue-shifted from their broad emission lines. Though these objects are believed to host the most powerful outflows of the BAL quasar subtypes, they exist in the early Universe, and so these objects are significantly understudied. I fit multi-epoch observations of the variable FeLoBAL J122933.32+262131.2 using the novel software package, *SimBAL*, which uses a spectral-synthesis forward-modeling procedure to effectively constrain physical parameters of the absorbing gas as a function of velocity. My aim is to obtain a detailed model of the BAL region for J122933.32+262131.2 that could help clarify the location and power of the outflow to determine its impact on the host galaxy.

1. INTRODUCTION

1.1. *Motivation*

A quasar is an extremely luminous active galactic nucleus (AGN) powered by a central SMBH and fed by a surrounding accretion disk. In this study, I aim to use spectroscopic observations of a quasar belonging to the most rare and powerful BAL quasar sub-class (FeLoBAL quasars) in order to constrain physical parameters of the windy outflow surrounding the central SMBH in these objects. Simulations of galaxy evolution indicate that outflows from AGN play an important role in the evolution of the host galaxy, so studying the dynamics of the most powerful AGN outflows can yield vital information regarding structures of the outflow and mechanisms for energy transfer. Though they do not dominate the general population of quasars, studying the unique intrinsic properties of Low-Ionization BAL (LoBAL) quasars can shed light on the sources of BAL variability and the nature of quasar outflows because of their characteristic strong outflow properties.

1.2. *Background*

1.2.1. *The Structure of a Quasar*

The central SMBH and the accretion disk, along with the broad line region (BLR), narrow line region (NLR) and the dusty torus, make up the major structural components of a quasar. Figure 1 illustrates our best understanding of the geometry of these components.

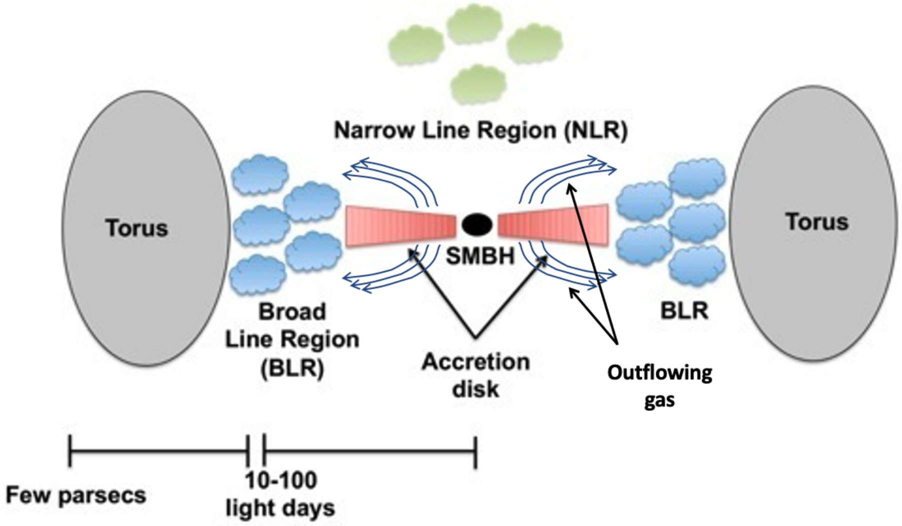

Figure 1. A schematic illustration of the prominent structural components of quasars. The accretion disk, a disk of swirling gas, falls towards the central SMBH. Surrounding these is a system of clouds known as the Broad Line Region (BLR), and further out, the dusty torus. Powerful outflows, or winds, are launched from the inner regions of the quasar and are illustrated by the blue arrows. Powerful radiation from the accretion disk forces surrounding matter away in the form of these winds. The Narrow Line Region (NLR) is another system of clouds surrounding the central quasar region. This figure was adapted from Ricci (2013).

It is generally agreed upon that a SMBH with a mass of approximately $10^6 - 10^{9.5} M_{\odot}$ lies at the centre of each AGN, acting as the quasar engine (Kormendy and Richstone 1995). Matter travelling towards the SMBH has considerable angular momentum relative to the black hole and will begin to form a disk surrounding the black hole instead of falling directly into it (Shakura and Sunyaev 1973). This accretion disk is geometrically thin but optically thick (Poludnenko et al. 2002), which means that photons are in thermal equillibrium with the gas. Matter in the accretion disk will follow Keplerian orbits around the black hole as gravitational and centrifugal forces balance each other (Shakura and Sunyaev 1973). Magnetorotational instability in the matter in a quasar's accretion disk gives rise to turbulence which results in a loss in angular momentum in the matter in the disk due to friction (Balbus and Hawley 1991). This instability results from the decrease in the angular velocity of the conducting matter in the accretion disk as it travels further from the inner regions of the disk (Balbus and Hawley 1991). The energy released from this accretion disk is given by

$$L_{\rm acc} = \frac{GM\dot{M}}{R}, \tag{1}$$

where M is the mass of the black hole and $\dot{M}$ is the rate of change of mass in the accretion disk, R is the distance of separation, and G is the gravitational constant (6.647×10^{-11} m^{3}kg^{-1}s^{-2}) (Frank et al. 2002). The outward release of such large amounts of energy can actually halt the process of accretion, slowing the growth of the central SMBH. This self-regulating mechanism is characterised by the Eddington limit, a balance between outward radiative forces and inward accretion forces given by

$$L_{\rm Eddington} = \frac{4\pi G c m_p M}{\sigma}, \tag{2}$$

where the c is the speed of light (2.998×10^5 km s), m_p is the mass of a proton (1.67×10^{-27} kg), and σ is the Thomson scattering cross-section (6.65×10^{-29}m^2, for an electron). In a black-body approximation, the temperature of the accretion disk as a function of radius is given by

$$\frac{GM\dot{M}}{2R} = 2\pi R^2 \sigma T^4, \tag{3}$$

(Peterson 1997).

The BLR refers to a system of clouds surrounding the central SMBH (Laor 2004). Continuum emission from the accretion disk that passes through these clouds is re-emitted in a roughly spherical manner, and is observed as broad emission lines characterized by physical parameters of the absorbing cloud (Gaskell 2009). For example, BLR clouds have high column densities, and will be highly ionized near the front of the cloud (region of the cloud closest to the accretion disk - the source of the ionizing continuum) and nearly neutral at the back of the cloud. A typical BLR cloud will have a density of about 10^{10} cm^{-3} and column density (the projected density of matter along the line of sight) of about 10^{23} cm^{-2} (Netzer 2013). Broad emission lines correspond to especially large line widths of order 1000 km/s due to Doppler broadening, which suggests that these clouds may exist in regions of high gravitational potential, making them good probes for the central regions of AGN (Peterson 2006).

The region of gas which exists beyond the BLR is the NLR, and emission from this region will be characterized by narrow spectral features (Peterson 1997). The NLR is believed to extend much farther from the central black hole than the BLR (Groves 2007), to distances of 50 pc (Unwin et al. 2008) [1]. At this large distance, sometimes the NLR is referred to as the extended narrow line region and is unobscured by the dusty torus unlike the BLR depending on the orientation of the quasar.

The torus (sometimes referred to as the "dusty torus") of an AGN is the dusty molecular region lying outside the accretion disk. Readers are referred to Figure 1 for a more thorough visualization of the structure of this region. The geometry of this region is generally uncertain.

Relativistic jets are observed as strong collimated streams extending from the poles of a quasar perpendicular to the plane of the accretion disk. These jets can contribute to powerful outflows from AGN (Fabian 2012). This is rarely the case for quasars with which this project is concerned, however, as these particular quasars (BAL quasars) are in a stage of feedback which does not involve jets (Fabian 2012).

1.2.2. *BAL Quasars*

A broad absorption-line quasar is a subclass of AGN characterized by broad spectroscopic absorption features which have been significantly blue-shifted from their broad emission lines (Knigge et al. 2008); they make up between 10% and 30% of the total quasar population (Trump et al. 2006). These broad absorption features result from high-velocity outflows (winds) from the quasar driven by radiation pressure from the continuum emission (Trump et al. 2006). Such defining absorption features are classified as broad or otherwise using the Balnicity Index (BI), given by

$$BI = -\int_{25,000}^{3000} 1 - \frac{f(V)}{0.9} C dV, \tag{4}$$

put forward by Weymann et al. (1991). The bounds of integration are measured in units of km/s, and represent line widths. An absorption feature is thus considered "broad" if it has a width of at least 3000 km/s. In Equation 4, $f(V)$ refers to the normalized flux as a function of the velocity displacement from line centre. The constant C is unity everywhere $f(v) < 0.9$, otherwise it is zero. If the BI of a quasar is >0 km/s, then the quasar is classified as a BAL quasar (Weymann et al. 1991).

From a study of 25 BAL quasars and 29 non-BAL quasars from the Large Bright Quasar Survey (LBQS), Weymann et al. (1991) determined that the emission-line properties of both types of quasars were very similar, solidifying the theory that BAL quasars and non-BAL quasars are not two intrisically different groups of objects. Any observed differences were small and were attributed to differences in viewing angles and/or in angular distribution of the

---

[1] A parsec (pc) is a unit used by astronomers to measure large distances. One parsec is equal to 3.26 light-years.

emission line fluxes. A surprising result of this study was the strong correlation found between the presence of Fe II emission and a high balnicity index. Weymann et al. 1991 concluded that the observed strong Fe II emission was coming from large clouds ablated off the dusty torus of the quasar which would interact with outflows to ultimately bring about broad absorption troughs contributing to the high balnicity index for the given quasar.

The Absorption Index (AI) is an alternative index which could be used to classify quasars as BAL or otherwise which was put forward by (Hall et al. 2002) in order to consider potential underestimation of the population of BAL quasars. This index is given by

$$AI = \int_0^{25,000} 1 - \frac{f(v)}{0.9} C dv, \tag{5}$$

where $f(v)$ is the normalized flux as a function of the velocity and the constant C is unity in regions where $f(v) < 0.9$ for at least 450 km/s and is zero everywhere else (Hall et al. 2002).

BAL quasars can be further classified into quasar sub-classes, depending on the specific spectral absorption lines detected which are ultimately determined from the physical properties (specifically ionization parameter and density) of the absorbing gas. BAL quasars with features from gases with high ionization energies, specifically C IV, are classified as High-Ionization BAL (HiBAL) quasars. The presence of low-ionization species such as Mg II together with high-ionization gases characterize Low-Ionization BAL (LoBAL) quasars. The final and most rare quasar sub-class contains those LoBAL quasars which also have excited-state Fe II or Fe III absorption lines. These are called Iron-Low-Ionization BAL (FeLoBAL) quasars (e.g. Trump et al. 2006). In terms of how much of the general quasar population is occupied by each of the BAL classes, Trump et al. (2006) found from a SDSS catalogue that about 26% are HiBALs, 1.3% are LoBALs, and 0.3% are FeLoBALs. These fractions are lower limits on their prevalence in the overall quasar population, as the unusual colors and strong absorption features make them less likely to be found in optical quasar surveys (Hewett et al. 2001).

BAL variability studies (like this one) involving LoBAL quasars, and particularly FeLoBAL quasars, are very valuable as the LoBAL sub-class of quasars in general is severely understudied. The FeLoBAL sub-class, which is the most rare of all quasar subtypes, is even more understudied. To date, most large-scale BAL variability studies have involved only High-Ionization BAL (HiBAL) quasars, which make up the majority of the quasar population and are most accessible to astronomers (e.g. Filiz Ak et al. 2013). The variability studies of LoBAL quasars which have been conducted have typically had small sample sizes, so the basis of inferences regarding the general quasar population on these samples is sometimes unreliable (e.g. Yi et al. 2019).

Lawther et al. (2018) observed a small sample of 4 FeLoBAL quasars and found that the FeLoBAL quasars they studied (and by extension, FeLoBALs in general) seem to represent an early stage of accretion driven by a recent merger event. In these cases, host galaxies are expected to show some kind of sign of an ongoing or recent merger.

FeLoBAL host galaxies may therefore have these signs which can be observed as starburst activity, evidence of an interacting companion galaxy, or even disturbed morphologies due to recent interactions. They were able to detect a companion galaxy for at least 1 and at most 3 of their studied galaxies, but were unable to determine whether each were undergoing or had recently undergone a merger. If all three suspected FeLoBALs were undergoing/had undergone merger activity in actuality, this 75% of their sample would be consistent with the merger fraction observed for non-BAL quasars in general for similar luminosities.

1.2.3. *AGN Feedback*

AGN feedback is defined as the process by which the energy and radiation released from accretion onto the central SMBH interacts with the interstellar gas of the host galaxy in order to determine the final stellar mass of the host galaxy bulge (Fabian 2012). Farrah et al. (2012) studied 31 reddened quasars with evidence for radiatively driven outflows in order to observe the relationship between outflows and the AGN as well as with starburst infrared (IR) luminosities. They find that there is a strong anti-correlation between the strength of a radiatively driven outflow and the contribution to the total IR luminosity of the quasar from star-formation. For systems with weaker outflows, the contribution to the IR luminosity from star-formation was 25% higher than observed in systems with stronger outflows (Farrah et al. 2012). Therefore, radiatively driven outflows appear to have a negative impact on star-formation in the host galaxies. The heating or ejection of interstellar gas due to powerful outflows could significantly reduce the materials available for star-formation (Fabian 2012). Growth of the central SMBH may also be halted, as the matter which would normally be accreted onto the SMBH will no longer be present (Fabian 2012).

There are two main feedback modes for quasars which depend on the accretion rate for the given quasar as well as the temperature of the gas involved. The “kinetic mode” refers to outflows in quasars accreting below the Eddington limit with abundances of hot gas (Fabian 2012). The resulting outflow is observed as strong radio jets. The “radiative mode” refers to outflows in quasars accreting close to the Eddington limit with an abundance of cold gas (Fabian 2012). This type of outflow is observed as a BAL wind (Fabian 2012).

Winds from quasars influence the quasar’s observed properties through processes such as ultraviolet (UV) line absorption, high-ionization line emission, reddening of lines in the optical and UV regimes, and X-ray absorption (Filiz Ak et al. 2013). Further, these winds contribute the growth of the SMBH and the evolution of the host galaxy as they remove angular momentum from the accretion disk of the quasar, thereby improving the efficiency of its accretion (Filiz Ak et al. 2013) and terminating/disrupting star formation in the host galaxy (Farrah et al. 2012).

1.2.4. *Physical Parameters of BAL Gas and BAL Variability*

Variability in BAL quasars is observed as changes in the BI of observed BALs as well as the appearance/disappearance of specific absorption lines, though the latter is less common (Leighly et al. 2015). BAL profile changes can provide insight into the structure of the outflow from a given BAL quasar as well as to the physical parameters of the gas when studied in the time domain (Barlow 1993). Since we are currently unable to spatially resolve the inner regions of BAL quasars, we rely on BAL variability to guide our understanding of the origins of their powerful outflows (Yi et al. 2019).

Equivalent width is a measure (in units of either wavelength or velocity) of the strength of an absorption or emission line. Equivalent width of a spectral line is defined as the width of a rectangle with height equal to the flux of the adjacent continuum, and width such that the area of the rectangle is equal to the area between the line and the continuum. It is a reflection of the change in flux relative to the continuum emission (Green 2020).

Column density refers to the amount of intervening matter between an observer and a given object along a line of sight. Column density is typically measured as the number of hydrogen atoms per square centimeter along the given line of sight, but other specific ions can be used for this measurement in the case of a highly-ionized gas. The column density is given by

$$N = \frac{m_e c}{\pi e^2 f \lambda} \int \tau(v) dv, \tag{6}$$

where $\tau(v)$ is the optical depth of the line (the opacity of the medium) which is a dimensionless quantity, m_e is the mass of an electron (9.109×10^{-28}g), e is the charge of an electron (4.803×10^{-10}cm$^{3/2}$g$^{1/2}$s^{-1}), λ is the wavelength of the line (measured in centimeters), and f is the oscillator strength (an expression of the probability that an electron is absorbed/emitted for a given transition) which is also a dimensionless quantity (Savage and Sembach 1991).

Covering fraction is another parameter which describes the geometry of how the absorbing gas interacts with the continuum and emission radiation. Covering fraction is the proportion of the resolved continuum source which is covered by the absorbing gas (Barlow and Sargent 1997). This proportion of coverage of the continuum source by the absorbing medium, sometimes referred to as "partial covering", can be observed in the structures of resulting absorption lines. For example, absorption lines may appear fully saturated (showing flat absorption structure near the line centre), yet do not reach zero flux at their minimum flux. From this, one might infer that the continuum source is actually larger than the absorbing region (Barlow and Sargent 1997). The structure of absorption lines which are present in quasar spectra are dependent on the physical location and velocity of the absorbing gas with respect to the continuum source (the accretion disk).

The ionization parameter of an absorbing/emitting gas refers to how highly ionized the species which make up the composition of the gas are. The ionization parameter (U) can be calculated using

$$U = \frac{n_\gamma}{n_e} = \int_{\nu_o}^{\infty} \frac{L(\nu) d\nu}{4\pi h r^2 n_e}, \tag{7}$$

(Barlow 1993). In Equation 7, the ionization parameter is represented as a ratio of the number density of hydrogen ionizing photons (n_γ) and the number density of free electrons (n_e); ν_o is the frequency of one photon with energy equal to 13.598 eV, r is the distance from the ionizing source, and $L(\nu)$ is the luminosity of the ionizing source (Barlow 1993). Under the assumption of ionization equillibrium, the ionization parameter can also be used to estimate the maximum distance from the absorber to the source (Barlow 1993).

The first large-scale BAL variability study was conducted by Barlow (1993). Their sample included 28 BAL quasars, 23 of which were observed over multiple epochs and 15 of which showed significant variability in the time domain. Using the time delays between the changes in the BALs and the continuum, it was concluded that changes in observed BALs were consequences of changes in the ionizing flux. Changes in the luminosity of the source would give rise to changes in ionization levels in the absorbing gas, assuming a constant number density for electrons (n_e). These time domain studies therefore allowed for constraint of the ionization parameter of the absorbing gas. By extension, the physical depth of the absorbing gas could be constrained by examining the time delay between observed changes in absorbing components which are closest/furthest to/from the continuum source (Barlow 1993).

Both short-term (4-9 month) and long-term (3.8-7.7 year) BAL variability studies in the time domain were performed by Capellupo et al. (2011), Capellupo (2012) and Capellupo et al. (2013) with a focus on the C IV BAL. Capellupo et al. (2011) and Capellupo (2012) found 39% of their quasar sample to be variable over shorter time scales, and 3% to be variable over longer time scales. They were able to deduce a characteristic time scale for variability to be less than a few years, and attributed observed variations to any combination of changes in ionization parameter of out-flowing gas and the movements of clouds across the line of sight to the quasar. They observed a larger likelihood for variability in objects observed over larger time scales with generally greater typical change in line strength for these objects compared to those observed over shorter time scales. Observed variations which took place over shorter time scales were targeted by Capellupo et al. (2013) to constrain the location of the out-flowing gas from the central SMBH. These variations were attributed to the "cloud crossing" model, and parameters of the clouds crossing the line of sight were constrained. For variations observed over the course of approximately 10 days, clouds were calculated to have crossing speeds of approximately $17 - 84 \times 10^3$ km/s at distances of $0.001 - 0.002$ pc from the central SMBH. For variations observed over relatively longer time scales on the order of months (less than a year), cloud crossing velocities were calculated to be on the order of 10^3 km/s at distances of about 1 pc from the central SMBH.

Filiz Ak et al. (2013) also found that BAL formation should take place within an order-of-magnitude within the radius from the central SMBH to which the out-flowing winds are launched. They used a sample of 291 quasars from the SDSS observed over a long time scale of $1 - 3.7$ years, and estimated that the average lifetime of a BAL trough along the line of sight was approximately a few thousand years. Ultimately, they concluded that the overall disappearance/appearance of BAL features is an extreme case of observed BAL variability as opposed to a distinct event. The results of their study were consistent with those found by Capellupo et al. (2011).

A multi-epoch BAL variability study was performed by (McGraw et al. 2015) on 12 FeLoBAL quasars over a range of redshifts spanning $0.7 \leq z \leq 1.9$ which were observed over timescales between approximately 10 days and 7.6 years. Out of the 12 FeLoBAL quasars analysed, 3 of which were confirmed to be variable. Operating under the assumption that the observed BAL variability was the result of motion of gas across the line-of-sight ("cloud crossing model", as mentioned earlier), the distance of the outflowing gas from the central SMBH was within 69, 7 and 60 pc for each of the variable quasars. These derived distances and timescales for variability were consistent with previous works (e.g. Hall et al. 2011; Vivek et al. 2012; Filiz Ak et al. 2013; Capellupo et al. 2013) and so it was concluded that the distance of outflowing gases in FeLoBAL quasars are generally located in a large range of distances from the central SMBH.

McGraw et al. (2018) used a sample of 71 BAL quasars with P V broad absorption in order to estimate outflow location and energetics. These estimations were based on the reasoning that the presence of P V BALs is indicative of C IV BALs (or others) which may be saturated such that the cloud-crossing model is most likely cause for variability. They constrain outflow distances to within $1 - 10$ pc of the central SMBH by considering changes in ionization, which is consistent with the results of Capellupo et al. (2013) and Filiz Ak et al. (2013). McGraw et al. (2018) put forward that variability in optically-thick C IV (detected at the same velocity as P V) supports the cloud crossing model, while variability in P V or Si IV BALs but not in optically-thick C IV supports the ionization-change model. They were able to constrain cloud crossing velocities to velocities greater than 1, 500 km/s. They were also able to conclude that outflows from BAL quasars were possible mechanisms for AGN feedback by estimating the kinetic luminosities of outflows in their sample ($0.001 - 1$ $L_{\rm bol}$) using hydrogen column density limits and calculated outflow distances.

The distributions of the distances between out-flowing gas and the central SMBH of BAL quasars and their kinetic luminosities were investigated using BAL variability studies by He et al. (2019) with a sample of 915 quasars from SDSS. They report outflow distances of tens of parsecs from the central SMBH, which are much larger than previously predicted. He et al. (2019) also present a new method for measuring this outflow distance using the BAL troughs with a focus on changes in ionization. They simulate BAL response to changes in ionizing flux and calculate the BAL equivalent width curve as a function of C IV column density for different equivalent widths.

A recent study on LoBAL quasar variability by Yi et al. (2019) involved multi-epoch spectroscopic observations of 134 quasars over both short and long time scales ranging from days to approximately 10 years. They are the first to report an observed time-dependent asymmetry in equivalent width variation such that weakening troughs outnumber strengthening troughs, and find that overall, the frequency of LoBAL variability is lower than that observed in HiBAL samples. They put forward a relationship between the observed BAL changes and the most likely cause for such a change. They find that the transverse-motion or cloud crossing scenario is dominant for strengthening BALs while changes in ionization are more likely to explain weakening BAL changes.

1.3. *Objectives and Methods*

I have fit the confirmed variable FeLoBAL quasar SDSS J122933.32 +262131.2 using *SimBAL* in order to model the absorbing gas in the BAL region. Multi-epoch spectra from the SDSS of 440 FeLoBAL quasars were analysed in order to determine whether or not they were variable sources and SDSS J122933.32 +262131.2 was chosen from this sample. Variation in absorption/emission features between epochs was inspected as well as variation in the high- and low-velocity components of absorption features. Variability was confirmed for SDSS J122933.32 +262131.2 with two epochs of data, both of which will be fit in this study.

I will be using the novel software *SimBAL* (Leighly et al. 2018) which uses non-conventional methods for spectral modelling for BAL quasars. As opposed to the traditional methods for absorption modelling, *SimBAL* does not require the identification of spectral lines in order to model absorption. In this case, line width and blending will not be provide the same challenges to the fitting of spectra in this study as they have historically. Instead, *SimBAL* constructs synthetic spectra from grids of parameter values calculated by a photoionization code *Cloudy* (Ferland et al. 2017) and then compares the synthetic spectrum to the observed spectrum using a Markov Chain Monte Carlo (MCMC) method in physical parameter space (Leighly et al. 2018). Further, as the spectral synthesis method adopted in *SimBAL* models the entire spectrum and not just identified present lines, the constrained model will reflect information from not only those lines which are present in the observed spectrum, but also those which are absent (Leighly et al. 2018).

The organization of information in this thesis is as follows. In Section 2 I discuss methodologies, including specifics regarding the fitting process. In Sections 3 and 4 I discuss primary results and constraining physical parameters from fits obtained using *SimBAL*. Section 5 will include a summary of main conclusions I draw from this study as well as an outline of future work.

2. MATERIALS AND PROCEDURES

Two epochs of spectroscopic observations for FeLoBAL quasar SDSS 122933.32 +262131.2 were fit using the spectral analysis software *SimBAL* (Leighly et al. 2018). Each epoch was initially fit manually in order to obtain a reasonable estimate of the physical parameters of the model. The quality of the initial fit as well as the initial positions of the walkers for the MCMC run were checked visually before the full MCMC algorithm was called (within *SimBAL*) using the high-performance computing consortium SHARCNET. The walker chains from the MCMC run were then sampled in post-processing, yielding parameter values and associated errors. The best-fit parameters were then used in a final calculation of the outflow radius, the distance from the central engine to the outflow being probed. This measurement helps to describe the structure and kinematics of the quasar outflow.

2.1. *Materials*

2.1.1. *Data*

A total of two epochs of spectroscopic observations of FeLoBAL quasar SDSS 122933.32 +262131.2 were obtained from the SDSS on the first epoch and from the Extended Baryon Oscillation Spectroscopic Survey (eBOSS), which were used over the course of this project. Both spectra had been redshift and galactic reddening corrected by Dr. Leighly, of the University of Oklahoma, before the processing in this project had begun. This object was selected from a sample of 440 FeLoBAL quasars, multi-epoch spectra of all of which were analysed in order to confirm or deny variability. The continuum flux levels as well as the strength of absorption features appeared to vary between epochs. These large differences are illustrated for a portion of both spectra in Figure 2 and certainly show promise of an interesting outflow model.

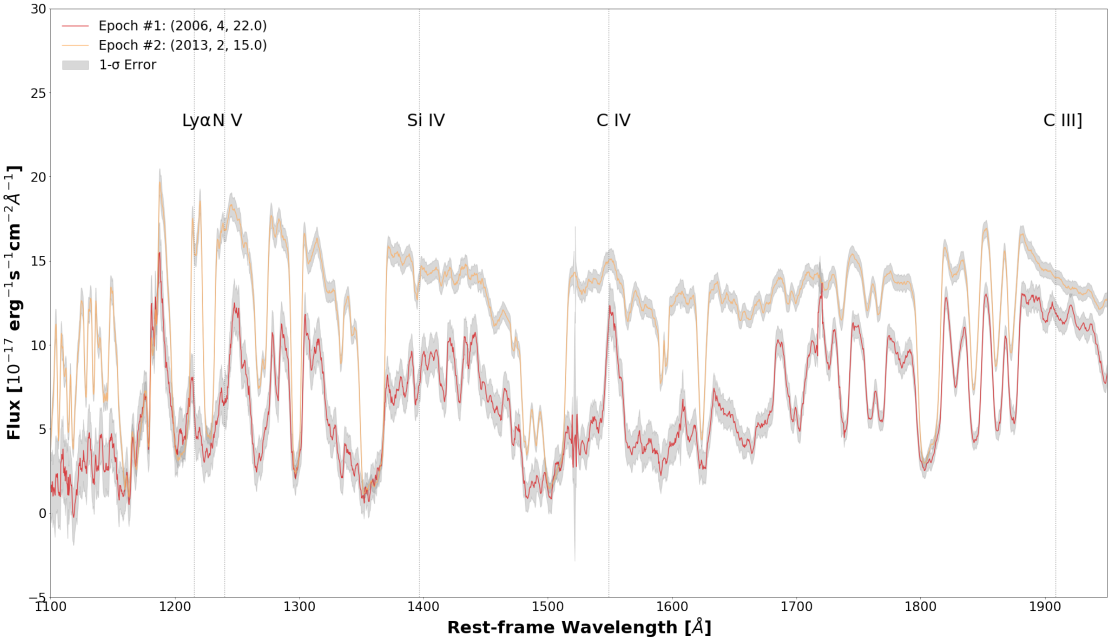

Figure 2. Two epochs of spectroscopic observations for FeLoBAL SDSS 122933.32 +262131.2 taken from the Sloan Digital Sky Survey are plotted with some prominant features labelled at the wavelengths at which they are known to occur (discrepancies between observed and theoretical wavelengths can be attributed to errors in redshift identification associated with the reduction pipelines used (SDSS and eBOSS pipelines)) in order to illustrate variability between epochs. The first observation which was taken on April 22, 2006 is plotted in red, and the second which was taken on February 15, 2013, is plotted in orange. The regions highlighting 1-sigma uncertainty are illustrated in grey for both epochs. There is clear variability between epochs. An obvious increase in continuum flux levels larger than uncertainties from the first to second epoch is visible as well as differences in widths and depths of absorption features between epochs. For example, notice the decrease in absorption in the high-velocity component (the absorption closest to the left-hand portion of the absorption trough) of the Si IV absorption trough from the first to second epochs while the absorption in the low-velocity component (the absorption closest to the right-hand portion of the absorption trough) appears to remain the same between both epochs.

2.1.2. *SimBAL*

SimBAL, is the software which was used in order to model the multi-epoch spectra for FeLoBAL SDSS 122933.32 +262131.2. *SimBAL* uses a forward-modelling Bayesian method in order to model spectra, a non-conventional BAL spectral analysis technique. A synthetic spectrum is constructed from grids of parameter values whch are calculated by the photoionizaiton code *Cloudy* (Ferland et al. 2017), and is compared to the data using a MCMC algorithm in physical parameter space. This method allows for the uncertainties of physical parameters to be extrapolated from posterior probability distributions along with the values of the physical parameters themselves. *SimBAL* is not yet publicly availible. Version C17 of *Cloudy* was used for this project, and readers are referred to Ferland et al. 2017 for further documentation on this software.

2.2. *Procedures*

A general overview of the fitting process is given, highlighting procedures for adjusting specific parameter values within *SimBAL*, followed by specific procedures in sections 2.2.1 and 2.2.2 for the individual spectra fitted in this project. Please see the Appendix for the relevant initial fits and output models from *SimBAL*. This section was included to illustrate the intermediate steps and decisions made in the fitting process for both epochs. In all cases, the fitting procedure began with the initial manual fitting process which involved selecting a set of initial physical parameter values that would produce a synthetic spectrum (from *Cloudy*) that could be compared to the observed spectrum by eye. Simple models such as those with one partial covering component (a single absorber for both continuum and line emission components of the spectrum) and spectral features modelled by Gaussian functions are best for initial fitting, and more complex components such as a top-hat model, for example, can be explored in the case where the Gaussian model is inappropriate for modelling absorption in the spectrum in question. Figure 3 illustrates how absorption features are modelled by a top-hat model, as this was the model which was adapted during the fitting process for both epochs. The initial fitting process was done through interaction with part of the *SimBAL* code implemented in Python and run through a series of Jupyter Notebooks. Jupyter Notebooks simplify the process of manually changing parameters and continually inspecting the quality of the initial fit being constructed. Once a suitable initial fit was achieved, the python code with the full implementation of *SimBAL* (including the MCMC algorithm) with the initial model as input is then passed to SHARCNET for execution.

2.2.1. *Spectral Modelling with SimBAL*

Overall, there are three primary parameters *SimBAL* uses to constrain the physical conditions of the probed gas. These include $\log(U)$, which is a dimensionless ionization parameter, $\log(n)$, which is the gas density measured in cm^{-3}, and $\log(N_H)$-$\log(U)$, which measures the column density of the gas slab with respect to the hydrogen ionization

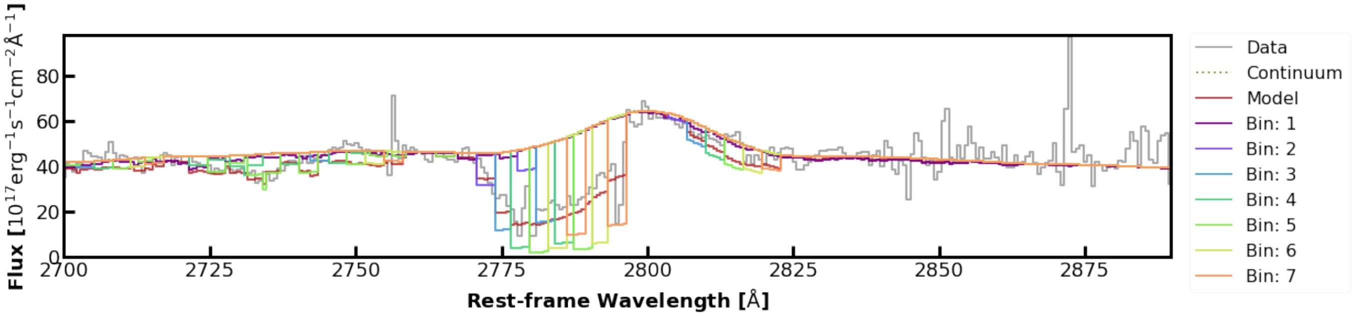

Figure 3. The different velocity bins for a single-component partial covering model with 7 top-hat bins are highlighted in different colors in order to illustrate how the top-hat model captures the shape of absorption lines such as Mg II (shown). This spectrum snippet is taken from part of the second observation of SDSS J122933.32+262131.2. The actual spectrum is plotted in solid grey, and the output model from 16000 simulations with *SimBAL* is given in red. The continuum component of this model is plotted in a broken grey line.

front, (Leighly et al. 2018). The covering fraction of the gas is modelled by *SimBAL* as the parameter log(a), where a is the exponent in the relationship

$$\tau = \tau_{max} x^a \tag{8}$$

(Leighly et al. 2018). Equation 8 is a parametrization of optical depth in which τ is the integrated opacity of the line, with $\tau_{\rm max} \propto \lambda f N({\rm ion})$, where λ is the wavelength of the line, f is the oscillator strength, and $N(ion)$ is the ionic column density (Savage and Sembach 1991). In Equation 8, x represents the projection of the continuum source normalized to one dimension, and scales between values of 0 and 1, exclusive (Leighly et al. 2018). In this power-law parametrization of opacity, a large value of the covering fraction index, log(a), corresponds to a lower amount of absorption of continuum emission by the gas. Constraining the values of these physical parameters is central to this project, as these allow for conclusions to be drawn about the physical and dynamical properties of the probed outflow.

Other parameters used by *SimBAL* which are necessary for constructing the synthetic model spectrum with *Cloudy* paramter grids are fit concurrently with those modelling the gas. The initial stages of fitting involves setting and adjusting these parameter values until a sufficient initial model for the observed spectrum is reached. This set of initial parameters serve as a starting place in parameter-space for the walkers in the MCMC run. The parameters describing the continuum such as the power law normalization and power law slope as well as those describing emission such as the emission line strengths, the eigenvector coefficients (a set of four eigenvectors are used by *SimBAL* to describe the general, large-scale shape of the spectrum), the emission line convolution, and the reddening were adjusted first before considering adding absorption to the model. First, the continuum is fit by adjusting the power law slope and normalization (must be a non-negative value) according to the observed overall shape while setting all emission parameters (emission line strength and convolution, reddening, and eigenvector coefficients) to zero. Once a sufficient continuum fit is achieved, emission can be added to the model by adjusting the emission line strength parameter, the value of which must also be a non-negative number. The eigenvector coefficients typically remain initially set to zero unless there is compelling evidence to set them otherwise. The emission line convolution and reddening can then be individually added to the model, the values of which should also be non-negative numbers.

Once the continuum and emission model components were sufficiently adjusted, parameters describing absorption such as the ionization parameter index ($\log(U)$), density index ($\log(n)$), column density index ($\log(N_H)$-$\log(U)$), outflow velocity offset, outflow velocity width, and partial covering were then added to the initial model. The opacity of the outflow is further parametrized as a function of velocity by the use of "bins" which together model velocity components of line features. Here, the outflow velocity offset is the offset of the velocity of the gas from rest, and the velocity width refers to the width of the velocity bin. The column density parameter has flexible upper and lower limits which are dependent on the values of the ionization parameter index and the density index. Density has hard upper and lower limits of 25 and 0, respectively, and should be adjusted at this point in order to fit the smaller absorption features and then adjusted further in order to fit the larger features. The remaining absorption parameters such as outflow velocity offset and width (both should be non-negative), ionization parameter index (should be between 0 and 90), and partial covering index (should be between -1.5 and 2.5, signifying full covering and near not covering, respectively) should be added and adjusted to fit the observed spectrum at this point.

At this stage, it is important to recognize that the initial synthetic spectrum should not necessarily be a good fit of the observed spectrum, but instead can be thought of as a suitable starting place for the *SimBAL* algorithm, namely for the MCMC run. This can be quantified by checking the initial positions of the walkers in physical parameter space with respect to their hard upper and lower limits (their priors). A prior, or prior probability distribution, in Bayesian statistics, refers to a probability distribution for a given variable before any other evidence is taken into account regarding what the actual distribution of the variable might be. In other words, it expresses known information about a given variable. If, given their priors, the initial positions of the walkers are physically sensical, meaning that no walker 'steps' outside of the physical limits for a given parameter (as described above), then this initial model can be used in a run with *SimBAL* in order to determine the best-fit model for the observed spectrum. Such runs, as mentioned earlier, were completed via SHARCNET for this project.

After the run with *SimBAL* has completed (and was successful), the output (the posterior probability distributions for each of the parameters of the best-fit spectrum as well as the acceptance for the model) are analysed in post-processing to check the quality of the fit as well as the uncertainties associated with best-fit parameters. Quality of fit is generally assessed by visually inspecting whether or not the output model captures the correct shape of absorption/emission features present as well as that of the continuum. In order to effectively capture the shape of an absorption or emission feature, the corresponding feature in the model must have the same equivalent width for all velocity components present in the line as well as occur at the same wavelength as the corresponding line in the data. A model line which is not as strong or stronger than that which it is modelling in the data, though it occurs at the same wavelength, for example, does not effectively model that line. A model which is able to effectively capture the shape of prominent absorption/emission features and that of the continuum, and is able to do so consistently across the entirety of the covered wavelength range, is deemed an effective model. Convergence of the model can easily be verified by examining the posterior probability distributions after each simulation performed in the run (the number of which is arbitrary, though larger numbers of simulations are generally favourable, as the walkers have longer time to explore parameter space and find the best-fit model). Each routine run with *SimBAL* in this project consisted of a round of 8000 simulations with 800 walkers. If the posterior probabilities have not converged, additional simulations with *SimBAL* may be required in order to improve the goodness of fit, or the initial model must be reconsidered. If convergence has been achieved, then post-processing may begin. Acceptance can be thought of as a measure of how well the walkers explored their parameter space. A higher acceptance value implies that there is a higher proportion of steps a walker is taking which result in an improvement to the model, a lower acceptance value would imply that the walkers spent a significant amount of the total steps taken in a very local parameter space, each of which did not improve the model significantly (Gelman et al. 1997). For the purposes of this project, an acceptance value of 0.1 was desirable (Foreman-Mackey et al. 2013).

It is during the post-processing that the estimated best-fit values of the parameters can be harvested from the output data from *SimBAL* along with their corresponding uncertainties. The dynamical properties of the probed quasar outflow can be established by using the best-fit physical parameter values from *SimBAL* in order to derive quantities such as the radial distance of the outflow from the central quasar engine and mass outflow rate, for example. The distance from the central SMBH to the outflow was derived in this project for both epochs.

2.2.2. *Fitting the First Epoch*

The first spectrum for SDSS J122933.32 +262131.2 is plotted in red in Figure 2. Note that there are not any significant emission features in this spectrum, which made the fitting process slightly more difficult in the initial steps as this created a challenge in identifying a suitable location for the continuum. The first model explored was one with a single partial covering component which used a single Gaussian in order to model absorption and emission (though not necessarily present) features. The Gaussian model did not sufficiently model the shapes of the absorption features, particularly the observed differences in high- and low-velocity components in present absorption features, and so a top-hat model was explored instead. The single-component top-hat model with 5 top-hat bins was able to more effectively capture the shape of the absorption features. Figure A.1 presents the initial models for both the single-component partial covering model with a Gaussian model for opacity and the single-component partial covering model with 5 top-hat bins to model opacity which were considered.

A two-component partial covering model with 9 top-hat bins was found to effectively model the spectrum for the second epoch, and so this prompted the exploration of the same model for the first epoch. There did not appear to be any significant improvements between the initial models for the single partial covering component top-hat model and the two-component partial covering top-hat model, and so both were given as input to *SimBAL* for 16000 simulations. After inspecting the converged models from these simulations, the two-component partial covering model was found to model both the continuum and absorption features better overall than the single-component partial covering model. The additional 4 top-hat bins in the two-component model likely explain the improvement in the absorption feature modelling over the single component partial covering model with only 5 top-hat bins. See Figure A.2 for both of these output best-fit models from *SimBAL*.

Close visual inspection of the output spectrum for the two-component partial covering model with 9 top-hat bins revealed that the first and last bins do not seem to be contributing to the opacity in the model, and should therefore be removed. Also, it appeared that the model was under-predicting opacity around 2200 Å and over-predicting opacity around 2400 Å (the model is struggling to model the heavy absorption in these regions from around 2200 Å to 2800 Å known as the "Iron Curtain") (H. Choi, personal communication, February 25, 2021). Inspection of the best-fit parameters of this output spectrum revealed that some top-hat bins had partial covering fractions approaching the upper limit for the parameter, meaning that the corresponding bins are not covering the line emission components. These observations lead to the conclusion that the two-component partial covering model might be inappropriate for this spectrum, and the single component partial covering model should be revisited. In this new model, there should be only 7 top-hat bins (removing the first and last bins which were not contributing to the model) and the absorber (BAL) should only be covering the continuum and not the line-emission.

The two-component partial covering model was tested one final time with only 7 top-hat bins, along with the new single-component partial covering model with 7 top-hat bins and the BAL not covering the line emission. The input parameters were also adjusted for both of these models, and the resulting synthetic spectra were passed as input to *SimBAL* for 8000 simulations each. During post processing for the two-component model, inspection of the model's acceptance was 0.05 which is low (though is expected to be lower generally for top-hat models), and the posterior probabilities had not quite converged, so this model was sent back as input to *SimBAL* for another 8000 simulations, with the walker step-size shortened (setting the parameter "a" in `emcee.EnsembleSampler()` to 1.55 from the default value of 2.0; readers are referred to (Foreman-Mackey et al. 2013) for more information on walker sampling used here) to improve acceptance. Post-processing analysis of acceptance and posterior probability distributions for the single-component 7 top-hat bin model revealed a much higher acceptance of 0.12 with posterior probabilities close to convergence (closer than they had been for the two-component partial covering model). This model was also sent back as input to *SimBAL* for another 8000 simulations with the walker step size shortened again by setting $a = 1.55$ in `emcee.EnsembleSampler()`. After the second set of simulations, post-processing revealed converged models for both the single- and two-component models. Visual inspection alone was not sufficient to determine the quality of fit for each epoch. Despite the efforts to increase the acceptance in both models, shortening the walker step-size here was found to have the opposite effect to that which was intended. For the two-component partial covering model, the final acceptance was 0.025, and the posterior probabilities had not yet fully converged. The acceptance of the single component partial covering model was also lower yet, 0.04, however the posterior probabilities had fully converged. Figure A.3 presents both of these output models after 16000 simulations.

2.2.3. *Fitting the Second Epoch*

The second spectrum for SDSS J122933.32 +262131.2 is plotted in orange in Figure 2. The wavelength region covered in this spectrum is extended further into bluer wavelengths than the first and includes Mg II emission at around 2800 Å. This key feature is an important benchmark for reference during the initial fitting process as well as the final inspection of converged models. As was the case for the first epoch, the first model to be explored for this spectrum was a single component partial covering model with a Gaussian model for opacity. As was expected, the Gaussian model did not sufficiently model the absorption or emission lines in this spectrum. Further, because the model spectrum seemed to be over-predicting opacity in the longer wavelengths (particularly blue-ward of about 2300 Å) and under-predicting opacity in the shorter wavelengths (particularly red-ward of about 2300 Å), a two-component partial covering model with 9 top-hat bins was the next logical model to explore for this spectrum. See Figure A.4 for the initial models from the single-component partial covering Gaussian model and the two-component partial covering 9 top-hat bin model. This initial model more effectively modelled the absorption and emission features observed as well as mitigated the opacity imbalance present in the initial single component partial covering Gaussian model. This initial model was then passed as input to *SimBAL* for 16000 simulations. Though an analysis of the acceptance and posterior probability distributions for this model did not yield alarming results (acceptance of 0.0275 and probabilities likely to soon converge), visual inspection of the model spectrum was sufficient to rule this model as inappropriate for this spectrum. The imbalance in opacity between long and short wavelengths is apparent in the resulting fit, especially in the poor fit of the Mg II absorption line. The best model for this epoch would be one that accounts for this observed imbalance.

In an attempt to improve the quality of fit in the two-component partial covering model as described above, the model was altered so as to illustrate a "scattering model". In such a model, scattered light (from the continuum source, potentially scattered off of a separate absorber) which was unabsorbed by the BAL is seen along our line of sight in the spectrum. This model was implemented by introducing two new physical parameters representing scattered light components for both continuum and line emission, which are added to their respective output model components from *Cloudy* before being reddened. This initial fit was passed as input to *SimBAL* for 8000 simulations, and the output model was found to be inappropriate for this spectrum. In another attempt to improve the quality of fit for the two-component partial covering model as described above, the eigenvector coefficients in the initial two-component partial covering model were each set to 1, which appeared to significantly improve the model's ability to model the Magnesium II line and the general opacity across all wavelengths. This model was also passed as input to *SimBAL*, and was found to be a significantly better model for the spectrum that that of the original two-component partial covering model with all eigenvector coefficients initially set to 0. This output model is given in Figure A.5, compared to the initial two-component partial covering model with the eigenvector coefficients set to 0.

In a similar way as was done for the first epoch, close visual inspection of the scattered two-component partial covering model revealed that the partial covering fraction parameter approached the upper bound for most bins, and the first and last top-hat bins did not seem to be contributing to the opacity of the model either. The single component partial covering 7 top-hat bin model in which the BAL is not absorbing line emission which was implemented for the first epoch should therefore also be employed for the second epoch as well (J. Choi, personal communication, February 25, 2021). The initial parameters for this model were altered in order to accomodate this new model, and the initial fit effectively captured the shape of the continuum and line features as well as mitigated the opacity imbalance issue. This model was passed to *SimBAL* as input for 16000 simulations. The original two-component partial covering model (with no scattering components, eignevector coefficients all initially set to 1) was modified so as to only have 7 top-hat bins as opposed to the original 9, as well as to shorten the steps of the walkers in parameter space as described in the previous Section 2.2.1 (the "a" parameter in `emcee.EnsembleSampler()` was set to 1.7 from the default value) in order to boost the acceptance slightly from 0.07. This initial model was passed as input to *SimBAL* as well for 16000 simulations.

Visual inspection of the output for both of these model from *SimBAL* is sufficient to see that both models effectively model this epoch. The two-component partial covering model with the changes as outlined above has improved the modelling of the absorption and emission features particularly well since the original run with *SimBAL*, though does not seem to model the spectrum as effectively as the new single-component partial covering model in which line emission is not absorbed by the BAL. The output spectrum from this model has significantly mitigated the opacity imbalance observed in previous models without sacrificing the quality of fit for absorption and emission features. To back up visual inspection, post-processing analysis reveals an acceptance in this single-component partial covering top-hat model of 0.125 with converged posterior probabilities. For the two-component partial covering top-hat model, the acceptance is 0.06 and the posterior probabilities are far from convergence. This low acceptance value in the two-component partial covering model coupled with the shape of the posterior probability distributions (not near a converged model) are sufficient evidence to rule out this model as the best fit for this epoch. The output models from *SimBAL* for both the two- and single-component partial covering models with 7 top-hat bins as described above are given in Figure A.6.

2.2.4. *Extracting Best Fit Parameters and Performing Final Calculations*

During post-processing, the values of the parameters associated with the best-fit models were extracted as along with their corresponding uncertainties. The output from a successful *SimBAL* run is a series of walker positions in parameter-space. Initially, the posterior probability distributions are inspected visually so as to identify the initial set of iterations during which time the walkers were finding the converged model in parameter space (these initial iterations as "warm-up" for the walkers). This "burn-in" region was removed from each of the output chains from the best-fit models for both epochs and the remaining output chains were used to extract the best-fit parameter values and their associated uncertainties. Each chain in parameter space was considered a small sample of best-fit parameter values with as many components as iterations in the chain. The best-fit value for each parameter was taken to be the median parameter value in each walker chain post-burn-in, and each corresponding 1σ and 2σ uncertainty interval were calculated for each.

After extracting the model parameter values, physical properties of the probed outflow such as the distance between the absorber and the central supermassive black hole could be derived. Equation 7 can be re-written instead as

$$U = \frac{Q}{4\pi R^2 nc}, \tag{9}$$

Choi et al. (2020) where Q is the number of photoionizing photons emitted per second by the central SMBH, n is the number density of photons, and c is the speed of light, and of course U is the ionization parameter. The values of U and n in this calculation are taken directly from the extracted model parameters from *SimBAL*. The value of Q in this equation is derived by integrating the spectral energy distribution (SED) over all wavelengths which are able to ionize hydrogen (those with energies greater than the ionization potential of hydrogen which is 13.6 eV). Using these extracted and derived values in Equation 9, the radius of the outflow from the central SMBH can be calculated.

3. RESULTS

The best-fitting models for the spectra from both epochs from *SimBAL* were found to be single-component partial covering models with 7 top-hat velocity bins. These converged models are plotted against the actual observed spectra for both epochs in Figure 4. The parameters which were allowed to vary with respect to velocity offset were the column density and covering fraction. Though the covering fraction was found to change slightly with velocity offset, the column density remained constant with velocity offset between bins. These parameters were both found to remain constant as functions of time between the first and second epochs. The ionization parameter and density of the gas were parameters which were held constant as functions of velocity offset, and this behaviour is clearly illustrated in Figure 5. It is also shown that there are significant changes in these parameter values as functions of time between epochs. According to the best-fitting *SimBAL* models, there is a high dimensionless ionization parameter of $1.30 \pm 3.1 \times 10^{-4}$ in the first epoch, which drops to $1.11 \pm 3.3 \times 10^{-5}$ in the second epoch. In contrast, the density of the gas is $8.0 \pm 1.2 \times 10^{-10}$ cm^{-3} in the first epoch, which decreases to $6.2 \pm 4.1 \times 10^{-10}$ in the second epoch. Across both epochs and across all velocity bins, the column density remains at approximately 23×10^{-3} cm^{-2}. The dimensionless covering fraction index varies monotonically in the first epoch with velocity offset, from 0.32 ± 0.18 to 0.60 ± 0.09, and but then less predictably with velocity offset in the second epoch. The covering fraction index in the second epoch starts and ends at around 0.52 in the second and seventh velocity bins, with decreasing values towards the central bins with a minimum value of 0.30 ± 0.02 in the fifth velocity bin. The covering fraction index in the first velocity bin of the second epoch (2.34 ± 0.06) is significantly higher than that of the others for the same epoch. The velocity offset in the best-fitting model in the first and second epochs are -2437 ± 24.3 km s^{-1} and -2952 ± 0.5 km s^{-1}, respectively. The velocity bin widths for the first and second epochs were also given by 302.56 ± 4.58 km s^{-1} and 341.51 ± 0.12 km s^{-1}, respectively.

The numerical values of the physical parameters from these converged models for each velocity bin as well as the derived radial distance of the outflow from the central quasar engine (R) for each epoch are given in Table 1 along with their corresponding 2σ uncertainties. The derived outflow radii for each epoch which were calculated using the best-fit parameters $\log(U)$ and $\log(n)$ from corresponding epochs with Equation 9. The outflow radii for the first and second epochs were calculated to be $6.46 \pm 2.30 \times 10^{-3}$ pc and $63.6 \pm 2.50 \times 10^{-3}$ pc, respectively. The change in the parameter values between epochs as functions of velocity offset are illustrated in Figure 5 along with their associated 95% confidence regions.

4. DISCUSSION

When using the MCMC method, it is important to address the fact that by setting the initial positions of the walkers in parameter space, as opposed to randomly setting their positions for example, bias can be introduced to the model. Exploration of parameter space using MCMC methods is computationally expensive, and so the initial positions of walkers are set in order to mitigate this. There is a very small chance however, that by setting the walkers in their initial positions in parameter space, I could be setting them close to a region which may correspond to a local

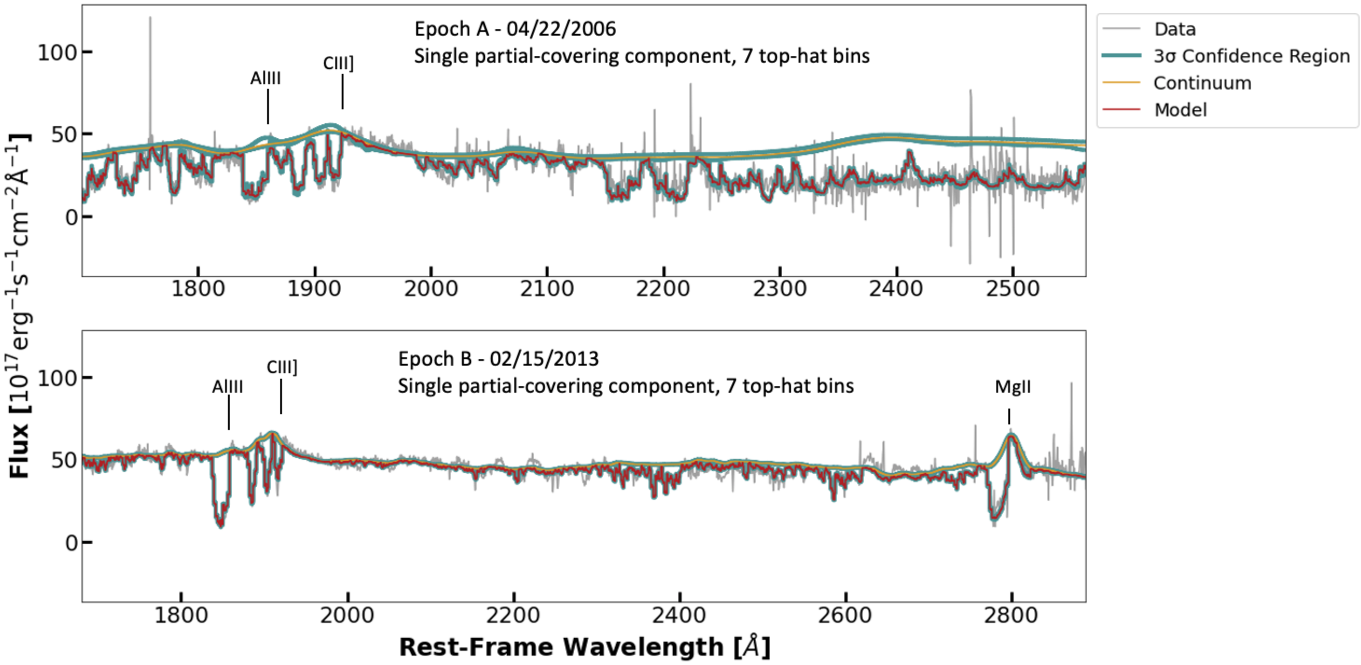

Figure 4. The best-fitting models for the first and second epochs are given in the top and bottom panels, respectively. The spectra are plotted as the flux from the outflow as a function of wavelength in the rest-frame of the quasar. These converged models each have a single partial-covering component and 7 top-hat bins to model spectral features. The model spectra are plotted in red, the model continua are plotted in yellow, and the 3σ uncertainty regions associated with each model component are highlighted in blue. The model spectra are each plotted over the corresponding observed spectrum for that epoch, which are given in grey. The differences in the wavelength ranges for each epoch are attributed to the differences in instrumentation used to take each spectra as they were taken as part of different spectroscopic surveys.

minimum in the posterior probability distribution in which they may become "stuck". In order verify that this is not the case, further analysis of the "best-fit" parameters must be explored. In the context of the spectral-fitting which was done in this project, this can be done by altering which parameters are changing with respect to velocity and/or time and verifying if the walkers are able to find a "best-fitting" model and whether or not this model is the same as the original.

The observed change in the ionization parameter between epochs is significant, from $1.301 \pm 3.10 \times 10^{-4}$ in the first epoch to $1.100 \pm 3.30 \times 10^{-5}$ in the second. This significant decrease in ionization parameter across epochs is consistent with the calculated increase in outflow radius which was derived from these values (from $6.46 \pm 2.30 \times 10^{-3}$ pc to $63.6 \pm 2.50 \times 10^{-3}$ pc across epochs). This derived change in radius which is increasing on the timescale of approximately 7 years (in the rest-frame of Earth), would be a powerful diagnostic for the dynamical processes which are at large in this probed outflow. As such, it is important that further analyses be conducted to verify that this result is robust to any bias or error in the derived best-fitting model.

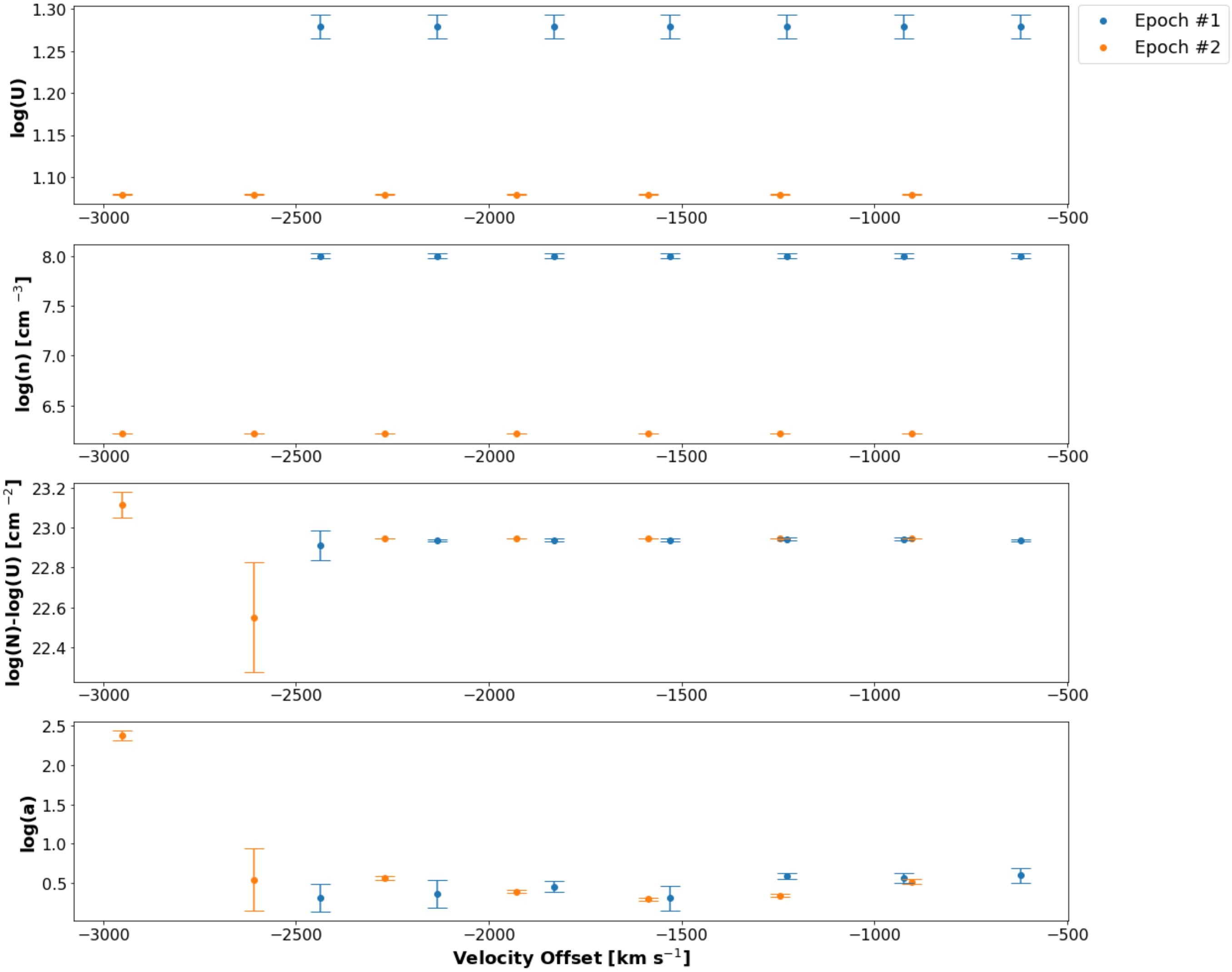

Figure 5. The extracted values of ionization parameter (top panel), density (second panel from the top), column density (third panel from the top), and covering fraction (bottom panel) are plotted for both epochs as functions of velocity offset. These values were extracted directly from the converged models from *SimBAL* for both epochs. The parameters from the first epoch are given in blue and those from the second epoch are given in orange. The error bars on the plot denote the 95% confidence region associated with each parameter value.

The covering fraction and the column density parameters were not found to be changing significantly with velocity or with time between epochs (relative to the changes observed between epochs in the density and ionization parameter). The first velocity bin for the second epoch (the gas of the outflow in the first epoch does not share this high-velocity component) appears to have a much larger value of covering fraction index than the other bins. This is most likely due to the walkers hitting the edge of the grid in which they can explore and becoming stuck here, as this value is close to the upper limit on this parameter. In order to confirm that this is not the true value of covering fraction for this velocity bin, experimentation with a different initial starting point for this parameter and an increased number of

Outflow Property	**Value for Epoch #1**	**Value for Epoch #2**
log(U)	1.301 $\pm 3.10 \times 10^{-4}$	1.100 $\pm 3.30 \times 10^{-5}$
log(n) [cm^{-3}]	8.003$\pm 1.20 \times 10^{-10}$	6.217 $\pm 4.10 \times 10^{-10}$
velocity offset [km s^{-1}]	-2437 ±24.3	-2952 ±0.5
velocity bin width [km s^{-1}]	302.56 ±4.58	341.51 ±0.12
log(N_H)-log(U) [cm^{-2}]	22.91 $\pm 7.40 \times 10^{-2}$ 22.94 $\pm 6.21 \times 10^{-3}$ 22.94 $\pm 6.39 \times 10^{-3}$ 22.34 $\pm 7.13 \times 10^{-3}$ 22.94 $\pm 6.34 \times 10^{-3}$ 22.94 $\pm 6.81 \times 10^{-3}$ 22.94 $\pm 6.33 \times 10^{-3}$	23.11 $\pm 6.61 \times 10^{-2}$ 22.55 ±0.28 22.95 $\pm 1.90 \times 10^{-4}$ 22.95 $\pm 1.73 \times 10^{-4}$ 22.95 $\pm 1.87 \times 10^{-4}$ 22.95 $\pm 1.73 \times 10^{-4}$ 22.95 $\pm 1.79 \times 10^{-4}$
log(a)	0.32 ±0.18 0.36 ±0.18 0.46 ±0.07 0.31 ±0.16 0.59 ±0.04 0.57 ±0.06 0.60 ±0.09	2.34 ±0.06 0.54 ±0.40 0.57 ±0.03 0.39 ±0.02 0.30 ±0.02 0.34 ±0.02 0.52 ±0.03
R [pc]	6.46$\pm 2.30 \times 10^{-3}$	63.6$\pm 2.50 \times 10^{-3}$

Table 1. Derived outflow properties from the best-fitting *SimBAL* model. The best-fitting *SimBAL* models for each epoch had single partial-covering components with 7 top-hat velocity bins. The outflow radius (R) is the only property which is not directly extracted from the *SimBAL* model, but is derived from U and n using Equation 9. All parameters are constant across each velocity bin except for log(N_H)-log(U) and log(a); in these cases the values for each velocity bin are given in order of increasing velocity offset.

simulations and/or a smaller walker step-size may help the walkers to avoid hitting this edge during their exploration of parameter space.

The other values of covering fraction index and column density which are constant in velocity-space will serve as good constraints on the physical processes which could be causing such large changes in ionization parameter and column density in the outflow over the course of the 7 years between epochs. In order to be able to draw such conclusions, further analysis must be done on the variability of the ionization parameter and density under the conditions where one of both of the two parameters are held constant with time while the other is allowed to vary independently. The results of such an analysis would also help to verify whether or not these best-fitting models truly are a good representation of the phenomena at hand. Further, since the column density parameter being fit with *SimBAL* is dependent on the ionization parameter, and the ionization parameter is observed to be changing in time according to these best-fit models, an analysis of how these parameters vary when one is held constant would also be important for determining the physical processes that cause these changes.

5. CONCLUSIONS AND FUTURE WORK

In conclusion, I was able to use *SimBAL*, a novel spectral analysis software, in order to constrain physical parameters of an outflow for FeLoBAL quasar SDSS J122933.32+262131.2 at two epochs in time. I successfully fit these two spectra using a single-component partial-covering model with 7 top-hat bins for both spectra. Using extracted values of the physical parameters from the best-fit models, I was able to derive a significant increase in the outflow radius between epochs. This radius was calculated to be $6.46 \pm 2.30 \times 10^{-3}$ pc on the first epoch, and $63.6 \pm 2.50 \times 10^{-3}$ pc on the second. This change between epochs allows for physical constraints of the location of the continuum source with respect to the gas. In order to confirm these dynamical changes, and confirm the physical mechanism which allows these changes to occur, further analyses of the best-fitting models must be performed. Such analyses would address which changes in parameter values would be responsible for the changes which are observed in the spectra. Once such analyses have been conducted, other quantitative outflow properties such as mass loss rate, momentum, and energy may also be derived from best-fitting parameters which would help to illustrate the large-scale, dynamical properties of quasar outflows which cause variability in their observed spectra, and further, to draw conclusions regarding the relationships of such outflows on their host galaxies.

6. ACKNOWLEGDEMENTS

Thank you to Dr. Karen Leighly for sharing these spectra with me, for your guidance and support, and for welcoming me into your group. Thank you to Joseph Choi of the University of Oklahoma for your discussion and guidance during the fitting process, specifically in the final stages. Thank you also to Cora and Julianna of the University of Oklahoma for your spectral-fitting expertise.

Thank you to Dr. Gallagher for your supervision and support throughout this project as well as through my undergraduate career. Thank you to Kaylie Green for your support, wisdom and patience with me throughout this project. Thank you to everyone in the Extragalactic group here at the University of Western Ontario for all of your feedback.

APPENDIX

The following figures depict the intermediate fits for various models which were explored throughout the fitting process for both epochs. These figures are included in order to illustrate any significant (or insignificant) changes which are observed in the output models from *SimBAL* as changes are made to the initial models. Please note that, as mentioned earlier, the wavelength ranges for the spectra for each epoch are not identical due to differences in the wavelength ranges of the instrumentation used in each instance. The first epoch was taken as a part of the SDSS and

Figure (panel)	**Epoch**	**Model Partial Covering Components**	**Opacity Profile**
A.1 (top)	1^{st}	1	Gaussian
A.1 (bottom)	1^{st}	1	5 top-hat bins
A.2 (top)	1^{st}	1	5 top-hat bins
A.2 (bottom)	1^{st}	2	9 top-hat bins
A.3 (top)	1^{st}	1	7 top-hat bins
A.3 (bottom)	1^{st}	2	7 top-hat bins
A.4 (top)	2^{nd}	1	Gaussian
A.4 (bottom)	2^{nd}	2	9 top-hat bins
A.5 (top)	2^{nd}	2	9 top-hat bins
A.5 (bottom)	2^{nd}	2	9 top-hat bins
A.6 (top)	2^{nd}	2	7 top-hat bins
A.6 (bottom)	2^{nd}	1	7 top-hat bins

Table 2. Relevant characteristics of the models illustrated in Appendix figures are summarized. Figures A.1 and A.4 illustrate depict input models while Figures, A.2, A.3, A.5, and A.6 depict output *SimBAL* models. Note that the major difference between models depicted in Figure A.5 is that the eigenvector coefficients of the initial model corresponding to the output model in the top panel were set equal to 0 and those of the initial model corresponding to the output model in the bottom panel were set equal to 1.

the second epoch was taken as a part of the eBOSS. Relevant model characteristics for each figure are summarized in Table 2 in order to clarify the differences between output models compared.

A. INTERMEDIATE FITS

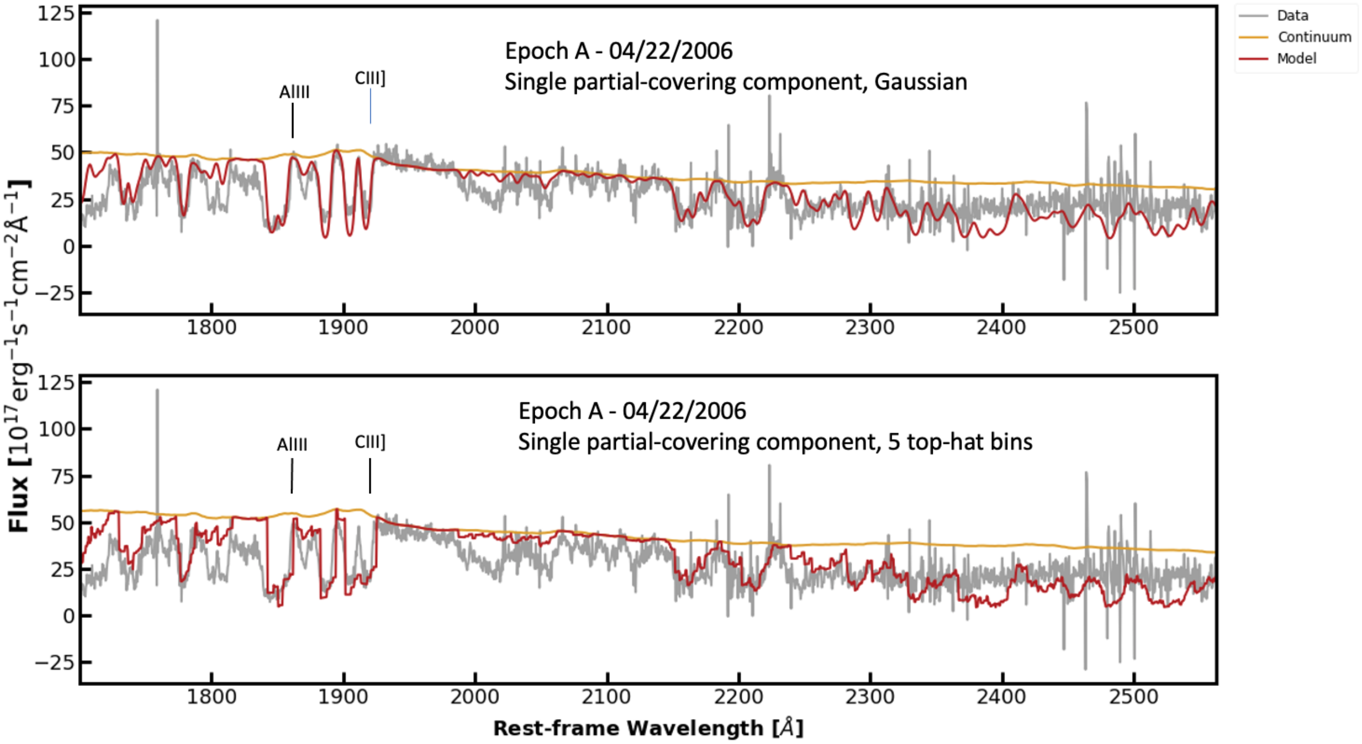

Figure A.1. The proposed initial models for the first epoch (observed spectrum is plotted in grey) are plotted in red, with their corresponding continua plotted in yellow. The top panel features the initial fit for the single-component partial covering model with a single Gaussian component modelling opacity. The bottom panel features the initial fit for the single-component partial covering model with 5 top-hat bins modelling opacity. The top-hat bin model for opacity can be seen to more effectively capture the shape of the components of the absorption features present than the Gaussian model.

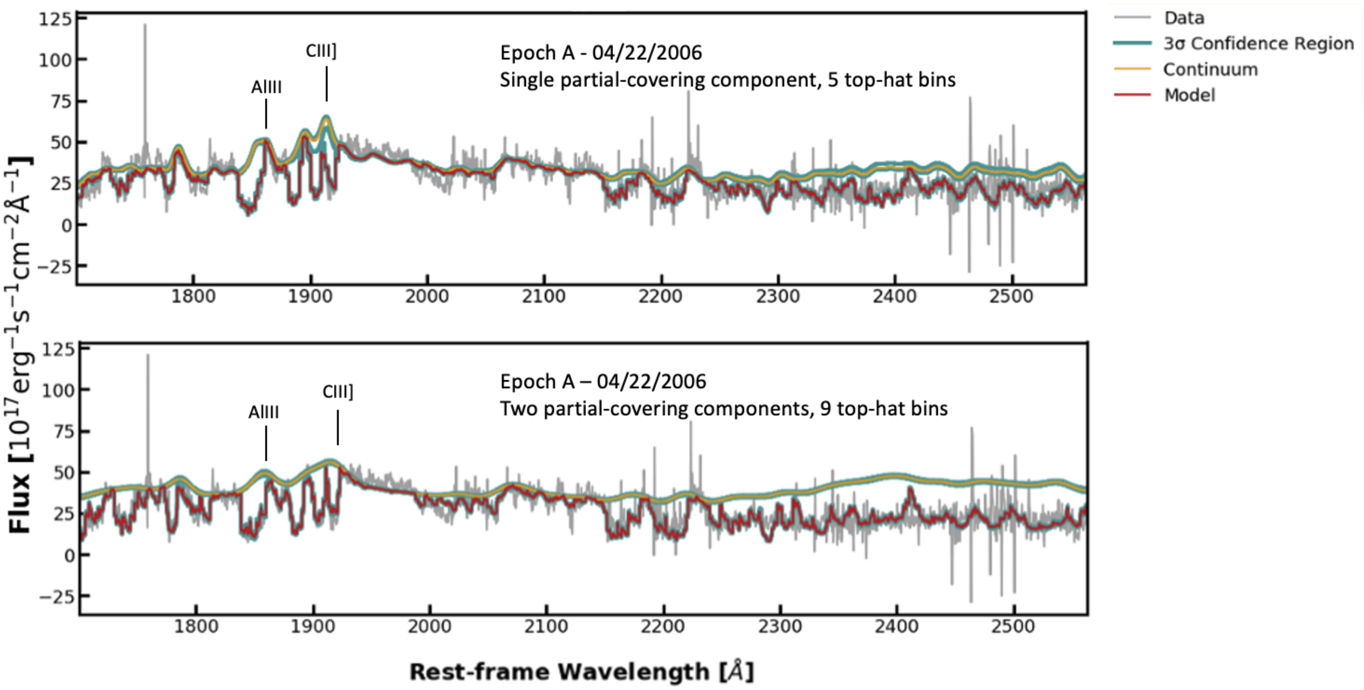

Figure A.2. The output models from *SimBAL* for the first epoch are given in red, their associated continua are given in yellow, and their associated 3σ uncertainty regions are highlighted in blue. The top panel features the single-component partial covering model with 5 top-hat bins to model opacity, and the bottom panel features the two-component partial covering model with 9 top-hat bins to model opacity. I opted to use more top-hat bins in the two-component partial covering model then in the single-component partial covering model in an attempt to better capture the shape of the absorption features present than was done by 5 top-hat bins in the first model explored (single-component partial covering). The two-component model appears to model the absorption features as well as the overall shape of the continuum more effectively than the single-component partial covering model. Both of these models were the result of 16000 simulations with 800 walkers with *SimBAL*.

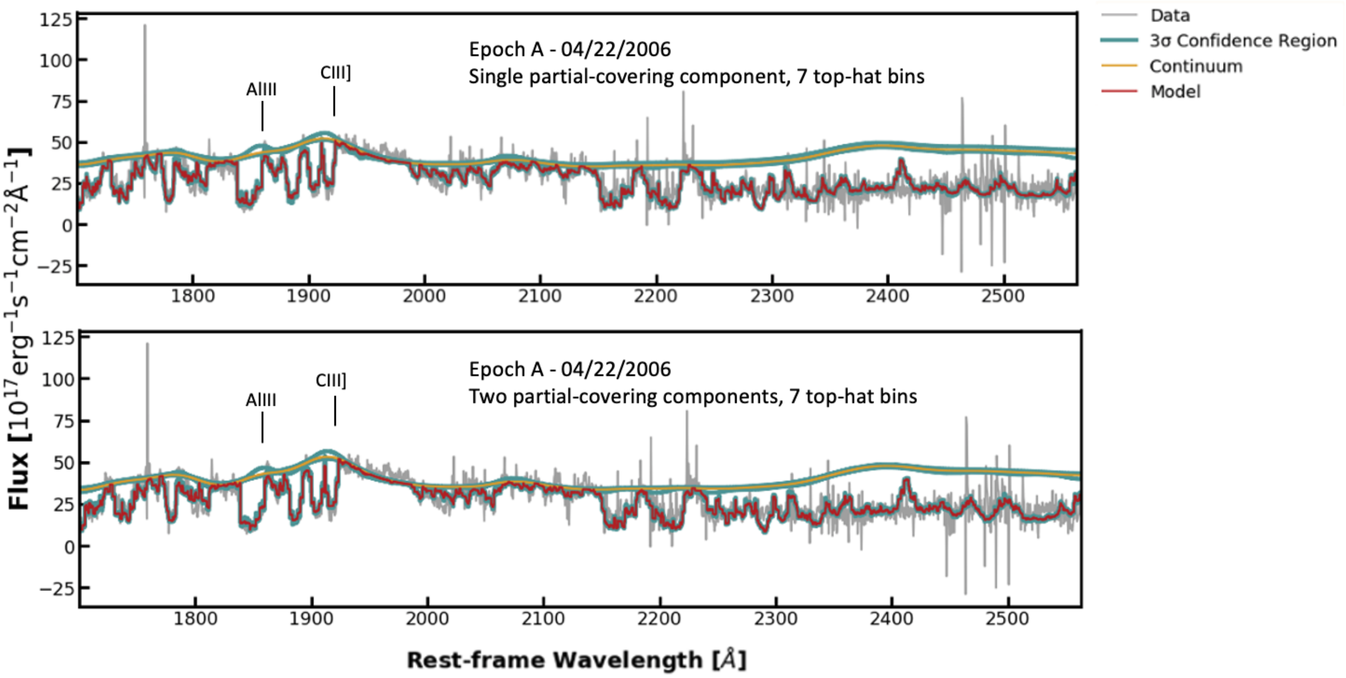

Figure A.3. The output models from *SimBAL* for the first epoch are given in red, their associated continua are given in yellow, and their associated 3σ uncertainty regions are highlighted in blue. The top panel features the single-component partial covering model with 7 top-hat bins, and the bottom panel features the two-component partial covering model with 7 top-hat features. In these models, 7 top-hat bins were explored as two of the bins in the 9 top-hat models which were explored previously were found to not be contributing to the opacity of the absorption line so they were removed. These output models were the both the result of 16000 simulations with 800 walkers with *SimBAL*. Visually, the models both seem to do an equivalently-effective job at fitting this epoch, however, the posterior probability distributions of the single-component model revealed that it may be the most appropriate model for this epoch of the two.

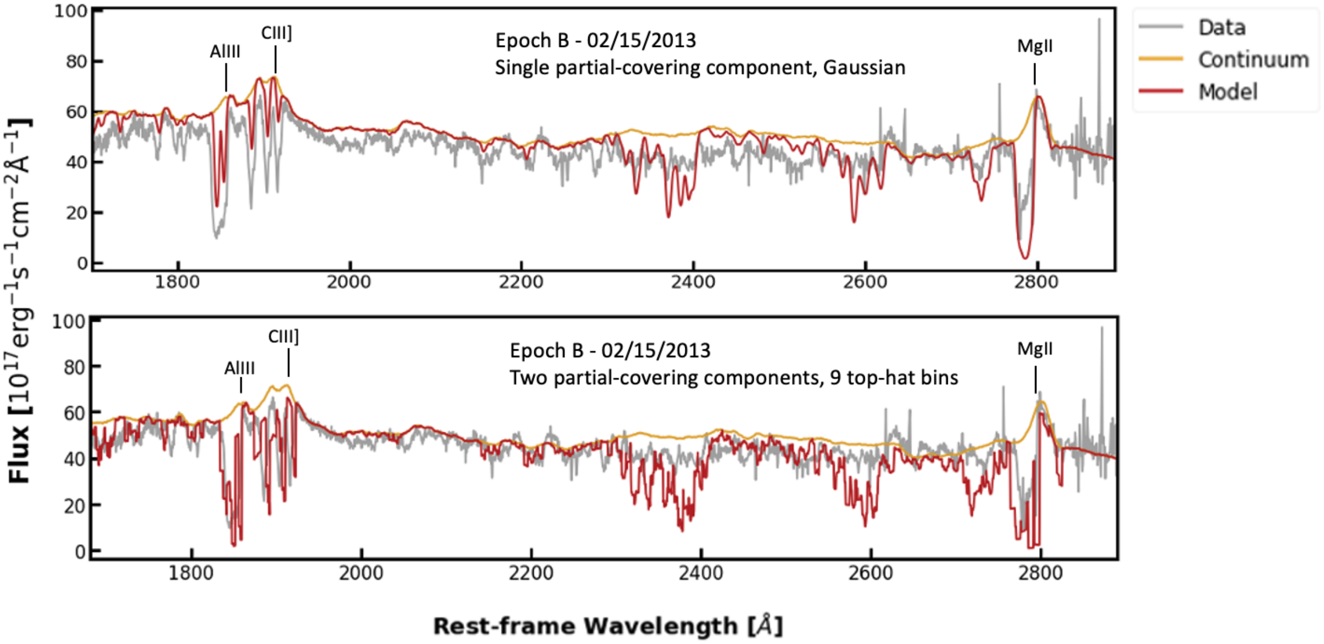

Figure A.4. The initial proposed models for the second epoch (observed spectra are plotted in grey) are plotted in red, and their respective continua are plotted in yellow. The top panel features the initial fit of the single-component partial covering model with a single Gaussian velocity component to model opacity. This model, as was the case for the equivalent model for the first epoch, does not effectively capture the shapes of the absorption and emission lines present, and as such was rejected for this epoch. The bottom panel features the two-component partial covering model with 9 top-hat bins, which can be seen to model the components of spectral lines more competently. In an attempt to remain consistent with the efforts of fitting the first epoch, I opted to experiment with 9 top-hat bins in this similar initial model for this epoch.

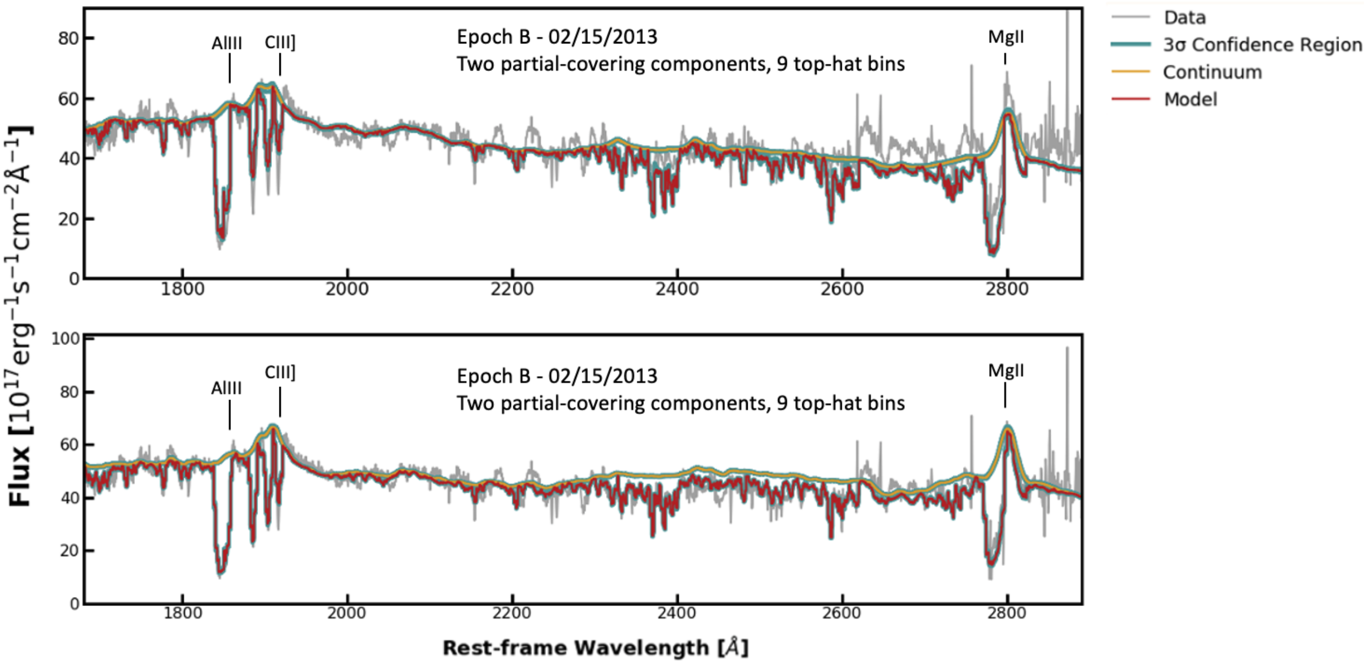

Figure A.5. The output models from *SimBAL* after 16000 simulations with 800 walkers for the two-component partial covering model with 9 top-hat bins are given. Here, 9 top-hat bins were explored further as an extension of the model explored in the bottom panel of figure A.4. The model spectra are plotted in red, their respective continua are plotted in yellow, and their associated 3σ uncertainty regions are highlighted in blue. The top panel illustrates the instance of the model in which the initial values of all four eigenvector coefficients are set to 0, and the bottom panel illustrates the instance of the model in which the initial values of all four eigenvector coefficients are set to 1. In the latter case, the imbalance in opacity in the model which is observed (that is to say, not predicting enough absorption in the shorter wavelength regions, and then over-predicting absorption in the longer wavelength regions) in the former case is mitigated, and as such these values were kept set to 1 in all initial models going forward for this epoch.

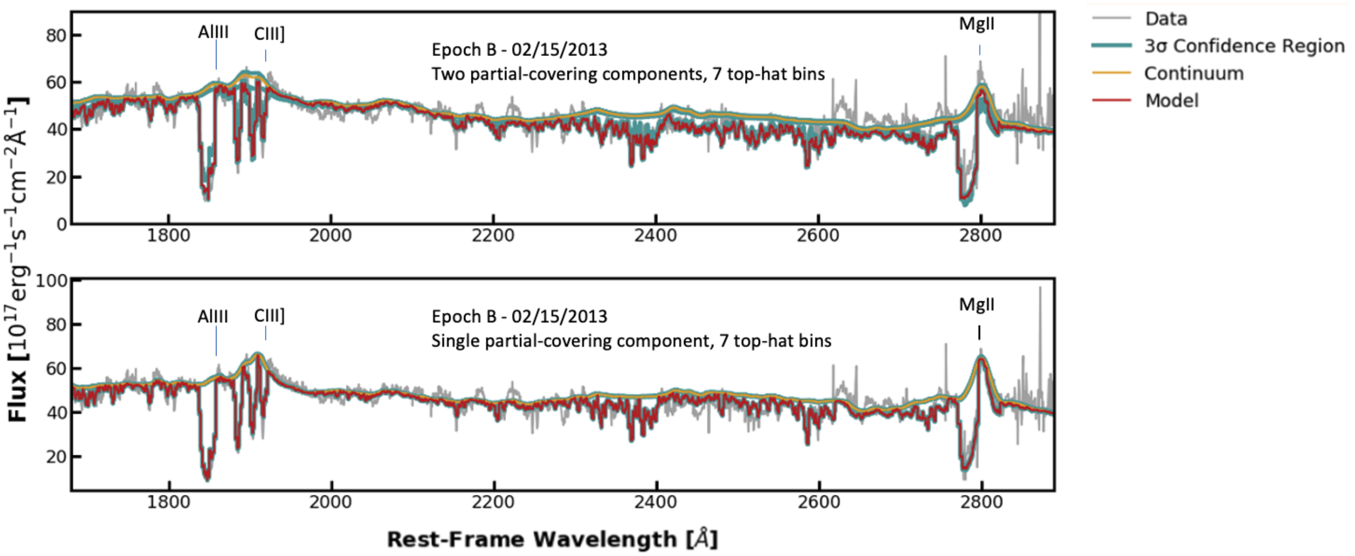

Figure A.6. The output models for the second epoch after 16000 simulations with 800 walkers in *SimBAL* are given for both the revised single-component partial covering model with 7 top-hat bins (bottom) and the two-component partial covering model with 7 top-hat bins (top). Here, 7 top-hat bins were used as two of the bins (the first and last) in the 9 top-hat bin models explored previously were found to not be contributing to the opacity of absorption lines (this was consistent to the models explored for the first epoch). The model spectra are given in red, their respective continua are given in yellow, and the associated 3σ uncertainty regions are given in blue. Not only does the single-component model more effectively model the Mg II feature as well as the spectrum in general than does the two-component model, but the high acceptance for the single-component model and its converged posterior probability distribution are evidence enough that this is the most appropriate model for this spectrum.

REFERENCES

C Ricci. Active galactic nuclei, 2013. URL http://www.isdc.unige.ch/~ricci/Website/Active_Galactic_Nuclei.html.

John Kormendy and Douglas Richstone. Inward Bound—The Search For Supermassive Black Holes In Galactic Nuclei. *ARA&A*, 33:581, January 1995. https://doi.org/10.1146/annurev.aa.33.090195.003053.

N. I. Shakura and R. A. Sunyaev. Reprint of 1973A&A....24..337S. Black holes in binary systems. Observational appearance. *A&A*, 500:33–51, June 1973.

A. Y. Poludnenko, E. G. Blackman, and A. Frank. Formation of Turbulent Cones in Accretion Disk Outflows and Application to Broad Line Regions of Active Galactic Nuclei. *arXiv e-prints*, art. astro-ph/0201398, January 2002.

Steven A Balbus and John F Hawley. A powerful local shear instability in weakly magnetized disks. i-linear analysis. ii-nonlinear evolution. *The Astrophysical Journal*, 376:214–233, 1991.

Juhan Frank, Andrew King, and Derek J. Raine. *Accretion Power in Astrophysics: Third Edition*. 2002.

Bradley M. Peterson. *An Introduction to Active Galactic Nuclei*. 1997.

A. Laor. What is the Broad Line Region? In Gordon T. Richards and Patrick B. Hall, editors, *AGN Physics with the Sloan Digital Sky Survey*, volume 311 of *Astronomical Society of the Pacific Conference Series*, page 169, June 2004.

C. Martin Gaskell. What broad emission lines tell us about how active galactic nuclei work. *New Astronomy Reviews*, 53(7-10):140–148, Jul 2009. ISSN 1387-6473. https://doi.org/10.1016/j.newar.2009.09.006. URL http://dx.doi.org/10.1016/j.newar.2009.09.006.

Hagai Netzer. *The Physics and Evolution of Active Galactic Nuclei*. 2013.

B. M. Peterson. *The Broad-Line Region in Active Galactic Nuclei*, volume 693, page 77. 2006. https://doi.org/10.1007/3-540-34621-X$_3$.

B. Groves. The Narrow-line Region: Current Models and Future Questions. In L. C. Ho and J. W. Wang, editors, *The Central Engine of Active Galactic Nuclei*, volume 373 of *Astronomical Society of the Pacific Conference Series*, page 511, October 2007.

Stephen C. Unwin, Michael Shao, Angelle M. Tanner, Ronald J. Allen, Charles A. Beichman, David Boboltz, Joseph H. Catanzarite, Brian C. Chaboyer, David R. Ciardi, Stephen J. Edberg, Alan L. Fey, Debra A. Fischer, Christopher R. Gelino, Andrew P. Gould, Carl Grillmair, Todd J. Henry, Kathryn V. Johnston, Kenneth J. Johnston, Dayton L. Jones, Shrinivas R. Kulkarni, Nicholas M. Law, Steven R. Majewski, Valeri V. Makarov, Geoffrey W. Marcy, David L. Meier, Rob P. Olling, Xiaopei Pan, Richard J. Patterson, Jo Eliza Pitesky, Andreas Quirrenbach, Stuart B. Shaklan, Edward J. Shaya, Louis E. Strigari, John A. Tomsick, Ann E. Wehrle, and Guy Worthey. Taking the Measure of the Universe: Precision Astrometry with SIM PlanetQuest. *PASP*, 120(863):38, January 2008. https://doi.org/10.1086/525059.

A. C. Fabian. Observational Evidence of Active Galactic Nuclei Feedback. *ARA&A*, 50:455–489, September 2012. https://doi.org/10.1146/annurev-astro-081811-125521.

Christian Knigge, Simone Scaringi, Michael R. Goad, and Christopher E. Cottis. The intrinsic fraction of broad-absorption line quasars. *MNRAS*, 386(3): 1426–1435, May 2008. https://doi.org/10.1111/j.1365-2966.2008.13081.x.

Jonathan R. Trump, Patrick B. Hall, Timothy A. Reichard, Gordon T. Richards, Donald P. Schneider, Daniel E. Vand en Berk, Gillian R. Knapp, Scott F. Anderson, Xiaohui Fan, J. Brinkman, S. J. Kleinman, and Atsuko Nitta. A Catalog of Broad Absorption Line Quasars from the Sloan Digital Sky Survey Third Data Release. *ApJS*, 165(1):1–18, July 2006. https://doi.org/10.1086/503834.

Ray J. Weymann, Simon L. Morris, Craig B. Foltz, and Paul C. Hewett. Comparisons of the Emission-Line and Continuum Properties of Broad Absorption Line and Normal Quasi-stellar Objects. *ApJ*, 373:23, May 1991. https://doi.org/10.1086/170020.

Patrick B. Hall, Scott F. Anderson, Michael A. Strauss, Donald G. York, Gordon T. Richards, Xiaohui Fan, G. R. Knapp, Donald P. Schneider, Daniel E. Vanden Berk, T. R. Geballe, Amanda E. Bauer, Robert H. Becker, Marc Davis, Hans-Walter Rix, R. C. Nichol, Neta A. Bahcall, J. Brinkmann, Robert Brunner, A. J. Connolly, István Csabai, Mamoru Doi, Masataka Fukugita, James E. Gunn, Zoltan Haiman, Michael Harvanek, Timothy M. Heckman, G. S. Hennessy, Naohisa Inada, Željko Ivezić, David Johnston, S. Kleinman, Julian H. Krolik, Jurek Krzesinski, Peter Z. Kunszt, D. Q. Lamb, Daniel C. Long, Robert H. Lupton, Gajus Miknaitis, Jeffrey A. Munn, Vijay K. Narayanan, Eric Neilsen, P. R. Newman, Atsuko Nitta, Sadanori Okamura, Laura Pentericci, Jeffrey R. Pier, David J. Schlegel, S. Snedden, Alexander S. Szalay, Anirudda R. Thakar, Zlatan Tsvetanov, Richard L. White, and Wei Zheng. Unusual Broad Absorption Line Quasars from the Sloan Digital Sky Survey. *ApJS*, 141(2):267–309, August 2002. https://doi.org/10.1086/340546.

Paul C Hewett, Craig B Foltz, and Frederic H Chaffee. The large bright quasar survey. vii. the lbqs and first surveysa, b. *The Astronomical Journal*, 122(2):518, 2001.

N. Filiz Ak, W. N. Brandt, P. B. Hall, D. P. Schneider, S. F. Anderson, F. Hamann, B. F. Lundgren, Adam D. Myers, I. Pâris, P. Petitjean, Nicholas P. Ross, Yue Shen, and Don York. Broad Absorption Line Variability on Multi-year Timescales in a Large Quasar Sample. *ApJ*, 777(2):168, November 2013. https://doi.org/10.1088/0004-637X/777/2/168.

W. Yi, W. N. Brandt, P. B. Hall, M. Vivek, C. J. Grier, N. Filiz Ak, D. P. Schneider, and S. M. McGraw. Variability of Low-ionization Broad Absorption-line Quasars Based on Multi-epoch Spectra from the Sloan Digital Sky Survey. *ApJS*, 242(2):28, June 2019. https://doi.org/10.3847/1538-4365/ab1f90.

D. Lawther, M. Vestergaard, and X. Fan. A Hubble Space Telescope imaging study of four FeLoBAL quasar host galaxies. *MNRAS*, 475(3):3213–3239, April 2018. https://doi.org/10.1093/mnras/stx3203.

Duncan Farrah, Tanya Urrutia, Mark Lacy, Andreas Efstathiou, Jose Afonso, Kristen Coppin, Patrick B. Hall, Carol Lonsdale, Tom Jarrett, Carrie Bridge, Colin Borys, and Sara Petty. Direct Evidence for Termination of Obscured Star Formation by Radiatively Driven Outflows in Reddened QSOs. *ApJ*, 745(2):178, February 2012. https://doi.org/10.1088/0004-637X/745/2/178.

Karen M. Leighly, Erin Cooper, Dirk Grupe, Donald M. Terndrup, and S. Komossa. Variable Reddening and Broad Absorption Lines in the Narrow-line Seyfert 1 Galaxy WPVS 007: An Origin in the Torus. *ApJL*, 809 (1):L13, August 2015. https://doi.org/10.1088/2041-8205/809/1/L13.

T.A. Barlow. PhD thesis, California University, 1993.

Kaylie Green. Investigating the Variability in Broad Absorption Line Quasars. 2020.

Blair D. Savage and Kenneth R. Sembach. The Analysis of Apparent Optical Depth Profiles for Interstellar Absorption Lines. *ApJ*, 379:245, September 1991. https://doi.org/10.1086/170498.

Thomas A. Barlow and W. L. W. Sargent. Keck High Resolution Spectroscopy of PKS 0123+257: Intrinsic Absorption in a Radio-Loud Quasar. *AJ*, 113:136, January 1997. https://doi.org/10.1086/118239.

D. M. Capellupo, F. Hamann, J. C. Shields, P. Rodríguez Hidalgo, and T. A. Barlow. Variability in quasar broad absorption line outflows - I. Trends in the short-term versus long-term data. *MNRAS*, 413(2):908–920, May 2011. https://doi.org/10.1111/j.1365-2966.2010.18185.x.

Daniel Moshin Capellupo. *Properties of quasar broad absorption line outflows*. PhD thesis, University of Florida, June 2012.

D. M. Capellupo, F. Hamann, J. C. Shields, J. P. Halpern, and T. A. Barlow. Variability in quasar broad absorption line outflows - III. What happens on the shortest time-scales? *MNRAS*, 429(3):1872–1886, March 2013. https://doi.org/10.1093/mnras/sts427.

S. M. McGraw, J. C. Shields, F. W. Hamann, D. M. Capellupo, S. C. Gallagher, and W. N. Brandt. Constraining FeLoBAL outflows from absorption line variability. *MNRAS*, 453(2):1379–1395, October 2015. https://doi.org/10.1093/mnras/stv1697.

Patrick B Hall, Konstantin Anosov, RL White, WN Brandt, MD Gregg, RR Gibson, RH Becker, and DP Schneider. Implications of dramatic broad absorption line variability in the quasar fbqs j1408+ 3054. *Monthly Notices of the Royal Astronomical Society*, 411(4):2653–2666, 2011.

M Vivek, R Srianand, P Petitjean, P Noterdaeme, V Mohan, A Mahabal, and VC Kuriakose. Probing the time variability of five fe low broad absorption-line quasars. *Monthly Notices of the Royal Astronomical Society*, 423(3):2879–2892, 2012.

S. M. McGraw, J. C. Shields, F. W. Hamann, D. M. Capellupo, and H. Herbst. Quasar outflow energetics from broad absorption line variability. *MNRAS*, 475(1): 585–600, March 2018. https://doi.org/10.1093/mnras/stx3219.

Zhicheng He, Tinggui Wang, Guilin Liu, Huiyuan Wang, Weihao Bian, Kirill Tchernyshyov, Guobin Mou, Youhua Xu, Hongyan Zhou, Richard Green, and Jun Xu. The properties of broad absorption line outflows based on a large sample of quasars. *Nature Astronomy*, 3:265, January 2019. https://doi.org/10.1038/s41550-018-0669-8.

Karen M. Leighly, Donald M. Terndrup, Sarah C. Gallagher, Gordon T. Richards, and Matthias Dietrich. The z = 0.54 LoBAL Quasar SDSS J085053.12+445122.5. I. Spectral Synthesis Analysis Reveals a Massive Outflow. *ApJ*, 866(1):7, October 2018. https://doi.org/10.3847/1538-4357/aadee6.

G. J. Ferland, M. Chatzikos, F. Guzmán, M. L. Lykins, P. A. M. van Hoof, R. J. R. Williams, N. P. Abel, N. R. Badnell, F. P. Keenan, R. L. Porter, and P. C. Stancil. The 2017 Release Cloudy. *RMxAA*, 53:385–438, October 2017.

A. Gelman, W. R. Gilks, and G. O. Roberts. Weak convergence and optimal scaling of random walk Metropolis algorithms. *The Annals of Applied Probability*, 7(1):110 – 120, 1997. https://doi.org/10.1214/aoap/1034625254. URL https://doi.org/10.1214/aoap/1034625254.

Daniel Foreman-Mackey, David W. Hogg, Dustin Lang, and Jonathan Goodman. emcee: The mcmc hammer. *Publications of the Astronomical Society of the Pacific*, 125(925):306–312, Mar 2013. ISSN 1538-3873. https://doi.org/10.1086/670067. URL http://dx.doi.org/10.1086/670067.

Hyunseop Choi, Karen M. Leighly, Donald M. Terndrup, Sarah C. Gallagher, and Gordon T. Richards. Discovery of a remarkably powerful broad absorption-line quasar outflow in sdss j135246.37+423923.5. *The Astrophysical Journal*, 891(1):53, Mar 2020. ISSN 1538-4357. https://doi.org/10.3847/1538-4357/ab6f72. URL http://dx.doi.org/10.3847/1538-4357/ab6f72.